Influence of configuration and microstructure on performance of La₂NiO₄₊δ intermediate-temperature solid oxide fuel cells cathodes

Nicolas Hildenbrand [a], Pieter Nammensma [b], Dave H.A. Blank [a], Henny J.M. Bouwmeester [a], Bernard A. Boukamp [a,*]

[a] *University of Twente, Dept. of Science and Technology & MESA Institute for Nanotechnology, P.O. Box 217, 7500 AE Enschede, The Netherlands*
[b] *Energy Centre Netherlands, P.O. Box 1, 1755 ZG Petten, The Netherlands*

HIGHLIGHTS

- Area specific resistance of La₂NiO₄₊δ (LNO) in symmetric cell lowest for $T_{sint} \sim 1000\ °C$.
- Microstructure dependence indicates role of surface diffusion of oxygen.
- Insertion of dense base-layer of LNO changes impedance from Gerischer dominated to thin layer type dispersion.
- Qualitative model explains the differences in impedance spectra and provides relation with oxygen exchange data.

ARTICLE INFO

ABSTRACT

The influence of sintering temperature on the polarization resistance of screen printed La₂NiO₄₊δ (LNO) cathodes is studied. The electrode dispersion is measured on symmetrical cells with a 100 μm 3% yttria-doped zirconia (TZ3Y) electrolyte and screen-printed yttria-doped ceria (YDC) barrier layers. The as-received commercial LNO powder was used in the formulation of the ink. For cathodes prepared following this procedure the optimum sintering temperature is 1000 °C. Analysis of the impedance spectra shows clearly a Gerischer dispersion (chemical impedance), with an activation energy of 124 kJ mol⁻¹ for the exchange rate parameter K_G. The addition of a dense LNO layer between electrolyte and porous electrode lowers the ASR by ~35%, showing a significant change in the oxygen transfer mechanism. A tentative model, based on a global two step oxygen exchange mechanism, is presented. There are also strong indications that surface diffusion of mono atomic oxygen is a major transport path. The electronic conductivity of LNO is too low at the intended operating temperature of ~600 °C, resulting in an additional resistance to the apparent electrolyte resistance.

1. Introduction

Intermediate-temperature solid oxide fuel cells (IT-SOFC) are potentially high-efficiency and low cost power generation systems. Because of their operating temperature around 600 °C, metal alloys such as stainless steels can be used as interconnects, significantly reducing manufacturing costs. The lower operating temperature requires more active cathodes than the state-of-the-art (La,Sr) MnO₃₋δ cathode. Cobalt-containing perovskites such as (La,Sr) CoO₃₋δ (LSC) and (La,Sr)(Co,Fe)O₃₋δ (LSCF) have been considered as very promising materials due to their high mixed ionic electronic conductivity and their good oxygen exchange kinetics. However, even at the operating temperatures of IT-SOFC, solid state and vapour phase chromium species transport from the interconnects to the cathode layer [1] and decrease the cathode activity for oxygen reduction, thus degrading the cathode's performance. Studies into the degradation mechanism of LSC and LSCF [2–6] have indicated that Sr-segregation from the bulk to the surface is playing an important role. At the cathode surface Cr reacts with Sr, resulting in the formation of several new phases: SrCr₂O₄, CoCr₂O₄, (Fe,Cr)₂O₃ and Cr₂O₃ [6]. Because of this chemical affinity of Cr for Sr and Co to form mixed oxides, a search for Sr- and Co-free cathode materials has ensued aiming at the development of cathodes with a significant higher resistance towards chromium poisoning.

Of interest are Ni-based mixed conducting materials, e.g. the Ruddlesden-Popper phases with the K₂NiF₄-type structure. Skinner et al. [7] showed that the oxygen tracer diffusion coefficient of

* Corresponding author.
  E-mail address: B.A.Boukamp@UTwente.nl (B.A. Boukamp).

lanthanum nickelate, $La_2NiO_{4+\delta}$ (LNO), is higher than that of LSM and LSCF, which indicates also high ionic conductivity for LNO. Several studies have been performed with $La_2NiO_{4+\delta}$ cathodes on different types of electrolytes, such as yttria stabilized zirconia (YSZ) [8–10] and cerium gadolinium oxide (CGO) [11]. In these studies on symmetric cells reasonable electrode performances were shown.

This work focuses on the optimization of LNO cathodes. First the influence of sintering temperature on the electrochemical performance of screen printed LNO cathodes is studied with impedance spectroscopy on symmetric cells. In previous studies on LSCF cathodes [11,12] it was found that the application of a dense and thin base-layer of LSCF, between electrolyte and porous electrode structure, gave a significant improvement of the cathode properties. Hence, in this study also the effect is studied of an additional thin and dense base-layer of LNO on the cathode performance. Thin base-layers were deposited by pulsed laser deposition (PLD) resulting in well-defined layers with full coverage of the electrolyte/electrode interfaces.

An obvious point of attention is the two-dimensional ionic conductivity of LNO [9] and its influence on the relation between microstructure and electrode performance. But also the rather limited electronic conductivity (with respect to LSCF) is a point of concern. The symmetric cells have been studied with electrochemical impedance spectroscopy (EIS), the cathode responses are analyzed in terms of an equivalent circuit, leading to more insight into the essential electrode processes. Finally, a tentative model is developed for the oxygen transport and transfer processes at the LNO cathode.

2. Electrode modelling

2.1. Gerischer impedance

Modelling of porous electrodes is, in general, rather complicated. However, in the case of a mixed ionic and electronic conductor (MIEC) often a well-defined transfer function can be used to analyze the impedance data. This function is known as the Gerischer [13] or chemical impedance [14,15] and is in principle a special case of unidirectional semi-infinite diffusion. The general form is easily derived from the basic diffusion equations and boundary conditions with a modification of the second law of Fick:

$$\frac{dC(x,t)}{dt} = \tilde{D}\frac{d^2C(x,t)}{dx^2} - K_G \cdot C(x,t) \qquad (1)$$

Here K_G presents the reaction rate of mobile species changing into immobile/inactive species or forming electrochemically inactive complexes [13]. $C(x,t)$ presents the concentration and $\tilde{D}$ the chemical diffusion coefficient of the mobile species, which diffuse along the x coordinate. The generic impedance expression for the Gerischer is given by:

$$Z_G(\omega) = \frac{Z_0}{\sqrt{K_G + j\omega}}$$

$$= \frac{Z_0}{\sqrt{2}}\left\{\sqrt{\frac{\sqrt{K_G^2 + \omega^2} + K_G}{K_G^2 + \omega^2}} - j\sqrt{\frac{\sqrt{K_G^2 + \omega^2} - K_G}{K_G^2 + \omega^2}}\right\} \qquad (2)$$

where Z_0 is proportional to $(\sqrt{D})^{-1}$ and contains all other material constants (see below). ω is the radial frequency, $\omega = 2\pi f$. The interesting point about the Gerischer impedance is that it shows a finite DC-value for a semi-infinite diffusion process:

$$Z_G(\omega = 0) = \frac{Z_0}{\sqrt{K_G}} \qquad (3)$$

In the high frequency range, the impedance of the Gerischer is identical to the well-known Finite Length Warburg (FLW), showing semi-infinite diffusion behaviour (Warburg: $Z_W = Z_0/\sqrt{j\omega}$). Below this range the shape of the Gerischer impedance is distinctly different from the FLW, showing a smooth curve-over to a (RC) type dispersion with the frequency of the maximum in $-Z''$ at: $f_{max} = K_G\sqrt{3}/2\pi$. Here the FLW shows an upturn from the Warburg behaviour towards a (RC) type dispersion.

Adler et al. [14] derived the chemical impedance for a porous $La_{0.6}Ca_{0.4}Co_{0.2}Fe_{0.8}O_{3-\delta}$ (LCaCF) cathode, where oxygen is reduced at the gas/solid interface and transported by solid state diffusion. For the LCaCF cathode the model gave a good match between the measured value and the calculated 'chemical resistance', R_{chem} ($=Z_G$ ($\omega = 0$)), obtained from the isotope exchange rate [16]. In a subsequent publication (Ref. [15]) the model was extended to include a competition between surface and bulk diffusion, leading to more complex relations for Z_0 and K_G. In this derivation it is assumed that the amount of oxygen adsorbed at the surface is negligible. After rearranging Eqs. (A-29, A-30) of Ref. [15] and using the same symbols, a detailed expression for the Gerischer impedance is obtained:

$$Z_0 = \frac{RT}{4F^2}\frac{1}{c_0x_v^0(1-\varepsilon)}\sqrt{\frac{A^0}{D_v(1+2\nu)}} \quad \left[\Omega \cdot cm^2 \cdot s^{1/2}\right] \qquad (4)$$

$$K_G = \frac{4A^0 a\Re_0}{c_0x_v^0(1-\varepsilon)} \quad \left[s^{-1}\right] \qquad (5)$$

where c_0 is the molar concentration of oxygen lattice sites, x_v^0 the mole fraction of oxygen vacancies (or in our case, x_i^0: excess oxygen) in equilibrium with the ambient. D_v is the vacancy diffusion coefficient with: $c_v \cdot D_v = c_0 \cdot D_O$ (D_O is the oxygen self-diffusion coefficient). A^0 is the thermodynamic factor: $A^0 = (1/2)(\partial \ln P_{O_2}/\partial \ln x_v)$, a is the surface area in [cm^2 cm^{-3}] and ε is the porosity. $\Re_0$ is the overall surface exchange rate of oxygen atoms in [mol cm^{-2} s^{-1}] and ν is the dimensionless ratio between surface diffusion and bulk transport. F, R and T have their usual meaning. For LNO the relation $c_i \cdot D_i = c_O \cdot D_O$ is used, with c_i the concentration and D_i diffusion coefficient of interstitial oxygen. The thermodynamic factor is expressed as function of the oxygen non-stoichiometry, δ: $A^0 = (1/2)(\partial \ln P_{O_2}/\partial \ln\delta)$.

One important restriction of the model developed by Adler is that only surface diffusion of neutral oxygen is assumed. Secondly, it is assumed that the electronic conductivity is high enough to impose no limitations on the oxygen exchange and diffusion processes. There are several strong indications that surface diffusion may occur by mono-atomic charged oxygen particles [17,18]. From isotope exchange experiments with gas phase analysis (following the time evolution of $^{16}O_2$, $^{16}O^{18}O$ and $^{18}O_2$) it has been suggested that the exchange process can be presented by two subsequent reaction steps: dissociative adsorption with possible partly charging, followed by bulk incorporation [19–21].

2.2. Dense layer impedance

In this study also thin, dense base-layers were used in the cathodes. Hence, it is important to consider the electrochemical properties of such a layer. In a recent publication, a derivation has been presented for the impedance of a thin and dense mixed conducting oxide layer [22]. This Generic Finite Length Warburg (GFLW) is given by:

$$Z_{\text{GFLW}}(\omega) = \frac{Z_0}{\sqrt{j\omega\tilde{D}}} \cdot \frac{\sqrt{j\omega\tilde{D}} \cdot \coth\ell\sqrt{j\omega/\tilde{D}} + k_{\text{exch}}}{k_{\text{exch}}\coth\ell\sqrt{j\omega/\tilde{D}} + \sqrt{j\omega\tilde{D}}} \tag{6}$$

With, for LNO:

$$\begin{aligned} Z_0 &= \frac{RT}{8F^2 \cdot c_0}\left[\frac{\partial\ln P_{O_2}}{\partial\ln c_0}\right] \\ &= \frac{RT \cdot V_M \cdot (1 + \delta/4)}{8F^2 S \cdot \delta}\left[\frac{\partial\ln P_{O_2}}{\partial\ln\delta}\right] \approx \frac{RT \cdot V_M}{8F^2 S}\left[\frac{\partial\ln P_{O_2}}{\partial\delta}\right] \end{aligned} \tag{7}$$

Here k_{exch} is the 'chemical' exchange rate in [cm s^{-1}], with $k_{\text{exch}} = A^0 \cdot \Re_0/c_O$. $\tilde{D}$ is the chemical diffusion coefficient in [cm^2 s^{-1}], ℓ the layer thickness in [cm] and S the surface area of the thin layer in [cm^2]. c_0 is the oxygen ion concentration in [mol cm^{-3}] which is related to the molar volume, V_M, by: $V_M = (4 + \delta)/c_0$. In the high frequency limit the well-known Warburg or semi-infinite diffusion impedance is obtained. For $\omega << \tilde{D}/\ell^2$ Eq. (6) can be represented by an (RC) circuit:

$$\begin{aligned} R_{\text{layer}} &= Z_0\left[\frac{1}{k_{\text{exch}}} + \frac{\ell}{\tilde{D}}\right], \quad \text{and} \quad C_{\text{app}} = \frac{1}{Z_0\left[\frac{1}{\ell} + \frac{k_{\text{exch}}}{\tilde{D}}\right]} \\ &= C_{\text{chem}}\frac{S \cdot \ell}{1 + \frac{\ell \cdot k_{\text{exch}}}{\tilde{D}}} \end{aligned} \tag{8}$$

C_{app} is the 'apparent capacitance' obtained from the impedance measurement, while C_{chem} is the specific redox capacitance in [F cm^{-3}] and is given by:

$$C_{\text{chem}} = \frac{8F^2}{RT \cdot V_M} \cdot \left[\frac{d\ln(P_{O_2})}{d\delta}\right]^{-1} \quad [\text{F} \cdot \text{cm}^{-3}] \tag{9}$$

The ratio $\ell \cdot k_{\text{exch}}/\tilde{D}$ determines how much of the redox process involves oxygen transport through the interface with the ambient or by direct supply through the electrolyte (battery electrode behaviour). The low frequency C_{app} can be used to estimate the distance from the electrolyte over which the battery behaviour is dominant.

2.3. Thermodynamic factor

From the previous sections on electrode modelling it is obvious that the thermodynamic factor is an important parameter. Its determination requires a quite different set of experiments. Here we will make use of literature values as reported by Naumovich et al. [23] and Kharton et al. [24]. In the latter publication a clear graph of δ vs P_{O_2} is presented for LNO. This graph has been analyzed graphically, extracting approximate $[P_{O_2}, \delta]$ values over the entire temperature (650–950 °C) and pressure range ($10^{-4} - 0.7$ atm). It turned out that almost all (P_{O_2}, δ) sets could be presented with an empirical formula (with T in K and P_{O_2} in atm):

$$\delta = \left(3.16 \cdot 10^{-6} \times T + 1.14 \cdot 10^{-3}\right) \cdot \ln(P_{O_2}) + \frac{87.8}{T} + 0.0199 \tag{10}$$

Except for pressures above 0.6 atm at 650° and 700 °C, the error in δ is well less than 0.5%. This relation will be used in the further analysis of the measurements. It is interesting to note that in the used $P_{O_2} - T$ range, ($d\ln(P_{O_2})/d\delta$) is independent of the oxygen partial pressure. Consequently C_{chem} will also be P_{O_2} independent, see Eq. (9). From the crystal lattice dimensions for LNO [25] the specific chemical capacitance in air at 600 °C is then calculated to be ~ 700 F cm^{-3}.

In many analysis of the impedances of SOFC-cathodes the electronic conductivity is assumed to be high enough so that it has no noticeable influence on the electrode processes. For LNO this may pose a problem as the electronic conductivity is significantly lower than found for e.g. LSCF. There are a few publications on the electronic conductivity of LNO [24,26]. For consistency we will also use the data published by Kharton et al. [24].

3. Experimental procedures

Symmetrical two-electrode cells were prepared at ECN (Petten, the Netherlands) by tape-casting and screen printing processes. Tape-casted yttria-partially stabilized zirconia (TZ3Y, Tosoh) was used as electrolyte [27]. Yttria-doped ceria (YDC, Praxair) was provided as interlayer by screen printing and sintered at 1400 °C on both sides of the tape-casted TZ3Y electrolyte. Next, two identical porous electrodes of La$_2$NiO$_{4+\delta}$ (LNO, CerPoTech, mean particle size 170 nm) were screen printed on both sides of the electrolyte, using a proprietary ECN homemade screen-printing ink. Samples with different microstructures were obtained by sintering at selected temperatures: 900 °C, 1000 °C or 1100 °C.

A second series of samples was provided with a dense LNO base-layer between electrolyte and porous electrode. These layers were deposited by pulsed laser deposition (PLD) on top of the YDC interlayers on both sides of the samples, prior to the screen-printing of the porous LNO electrodes. The pulsed laser deposition was performed with a KrF excimer laser, using a fluency of 1.5 J cm^{-2} and a frequency of 10 Hz. The LNO target was provided by placing an isostatically pressed LNO pellet on a rotating holder. The laser ablation occurred in a vacuum chamber in 0.02 mbar oxygen ambient, with a distance of 50 mm between target and substrate. The YDC/TZ3Y/YDC substrates were heated to 850 °C during deposition. Two samples were prepared with 200 nm thin layers on both sides, and two more samples with respectively 400 nm and 800 nm thin layers on both sides. After deposition of the porous electrode structures by screen printing, the cells were sintered at 1000 °C.

A schematic representation of the two different sample types, with and without a dense LNO base-layer, is presented in Fig. 1. Electrochemical characterization of the cells was performed at open-circuit voltage using a Pt grid (85.5 mesh) as current collector. The temperature dependence was measured in synthetic dry air between 800 and 300 °C at 50 °C intervals. At 600 °C the oxygen partial pressure dependence was measured between 0.01 and
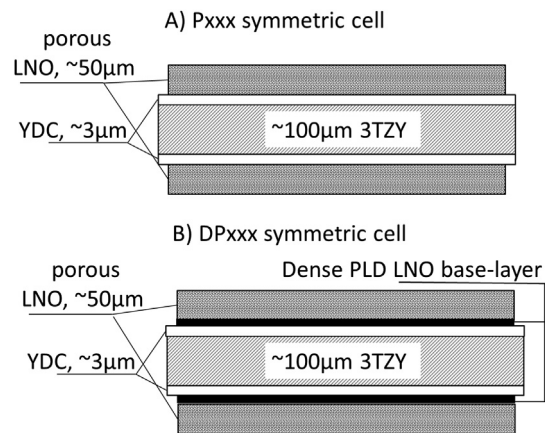

Fig. 1. Schematic arrangement of the symmetric cells. The YDC barrier layers are prepared by screen printing. The dense LNO base layers are prepared by pulsed laser deposition (PLD).

0.8 atm. The impedances were obtained with a Solartron 1250 FRA combined with a 1287 electrochemical interface over a frequency range of 65 kHz to 10 mHz in a pseudo 4-electrode set up (separate current and voltage probe leads). The applied ac-voltage was 10 mV (rms). The impedance data were validated with a Kramers–Kronig test program [28] and analyzed with the Complex Nonlinear Least Squares (CNLS) software package: 'Equivalent Circuit' [29,30].

4. Results and interpretation

4.1. Microstructural analysis

Fig. 2 shows SEM micrographs of the deposited and sintered cathode layers for the set of porous electrodes. From these it can be concluded that an increase in sintering temperature leads to larger and better connected crystallites. It is important to note that the microstructure is built up mostly from separately connected single crystals with an average size ranging from 255 nm ($T_s = 900$ °C) to 565 nm ($T_s = 1100$ °C). Further visual inspection also suggests that, with increasing sintering temperature, the number of 'singly attached' crystallites (dead-ends for conduction) is reduced. The crystallite orientation is random, as is also confirmed by XRD-analysis. This will lead to a significant number of miss-orientations of oxygen conduction planes at the grain boundaries, effectively blocking oxygen transfer. As a result the oxygen ion transport through the grains will be limited to a few grains adjacent to the electrolyte/electrode interface. This will also restrict the oxygen transfer between gas phase and bulk to an active layer of a limited number of grains.
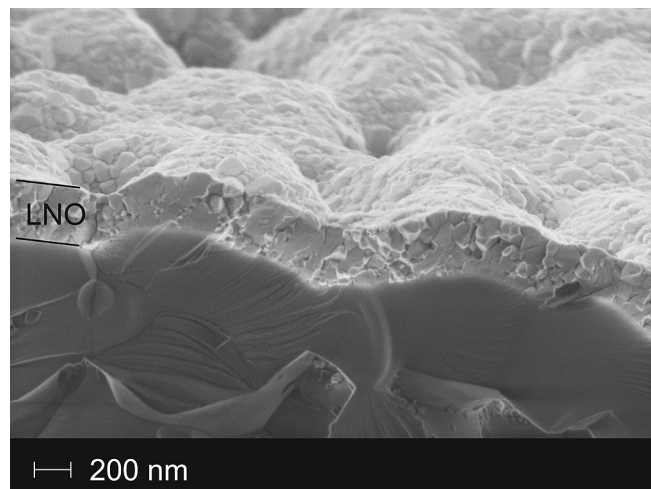

Fig. 3. SEM micrograph of the cross section of a 400 nm PLD–LNO layer prior to screen-printing of the electrode.

The two samples with a 200 nm LNO base-layer are denoted as DP200-A and DP200-B. SEM analysis indicated that the 200 nm layers were discontinuous, due to the rough surface of the screen printed YDC barrier layers. For both the 400 nm and 800 nm cells (denoted by DP400 and DP800) the dense base-layer proved to be completely dense. Fig. 3 shows the cross section of a 400 nm dense base-layer. Fig. 4 shows the XRD pattern as deposited, and after
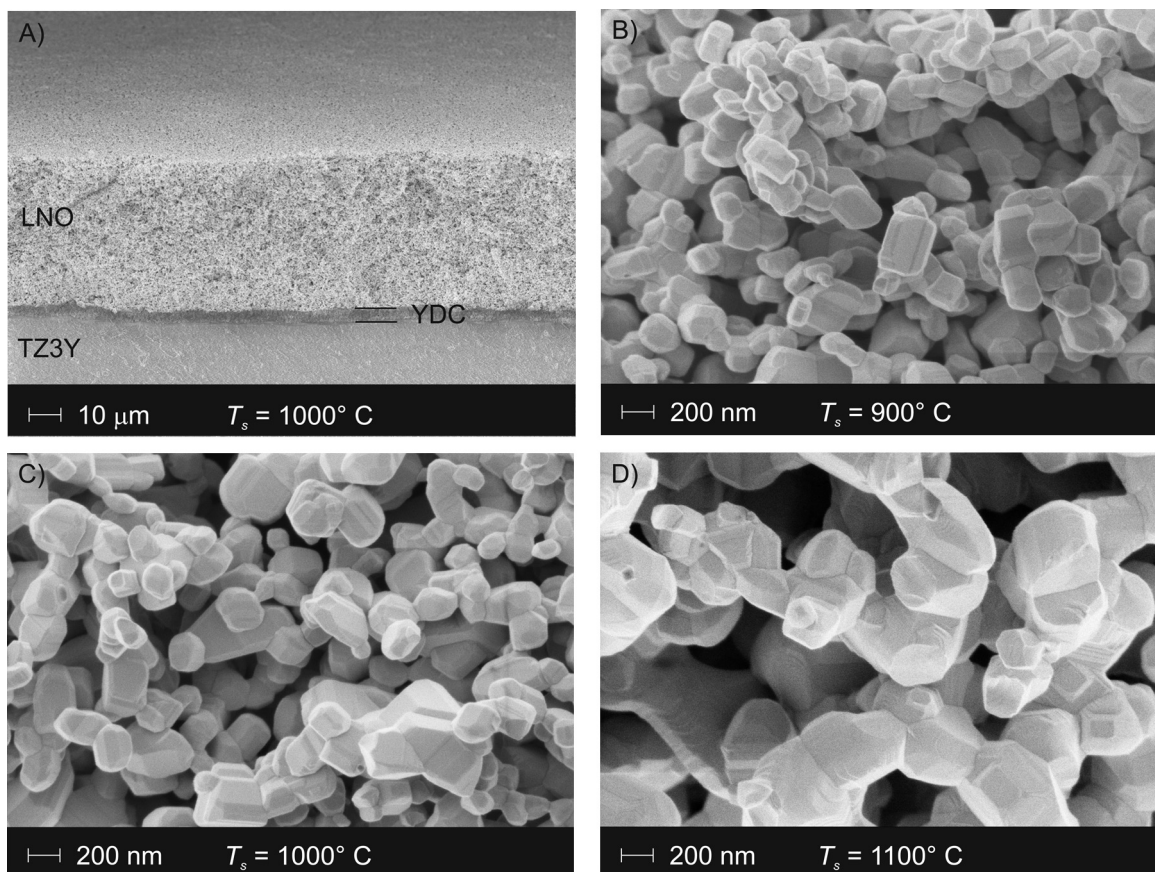

Fig. 2. A) SEM micrographs of a cross section of the symmetrical cell sintered at 1000 °C. SEM micrographs of the microstructure of a LNO porous cathode sintered at: B) 900 °C, C) 1000 °C and D) 1100 °C.
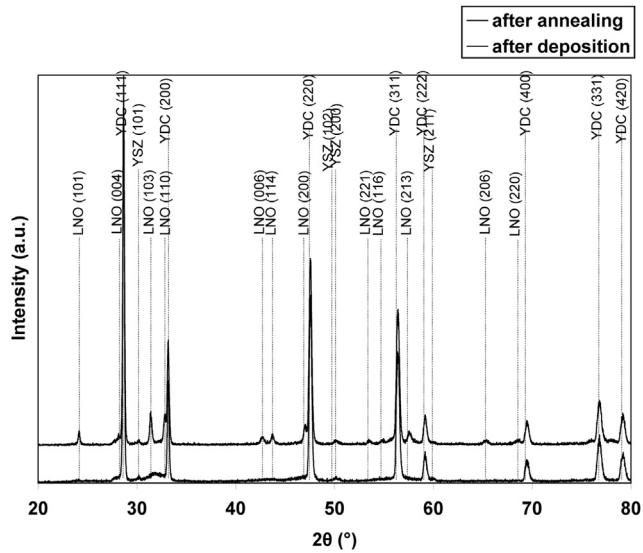
Fig. 4. XRD patterns of the symmetric LNO/YDC/YSZ sample, directly after pulsed laser deposition (lower curve) and after annealing at 900 °C (upper curve).

annealing at 900 °C. Upon annealing the LNO layer becomes nano-crystalline ($d < 100$ nm) with a random orientation of the crystal grains.

4.2. Impedance of porous cathodes, temperature dependence

Four symmetrical cells, sintered at 900 °C (cell P900), 1000 °C (two cells, P1000-A and P1000-B) and 1100 °C (cell P1100) were studied. Fig. 5 presents the normalized impedances measured at 600 °C in synthetic air. The apparent electrolyte resistance and instrumental inductance were subtracted from the data set. The dispersions are quite featureless, but CNLS-analysis clearly showed the presence of a Gerischer dispersion in series with a (RQ) type dispersion, i.e. a parallel combination of a resistance and a CPE (constant phase element or Q-element: $Y_Q(\omega) = Y_0(j\omega)^n$). The frequency power dependence of this CPE is around 0.5, which indicates that it is most likely related to a diffusion process. In Fig. 6
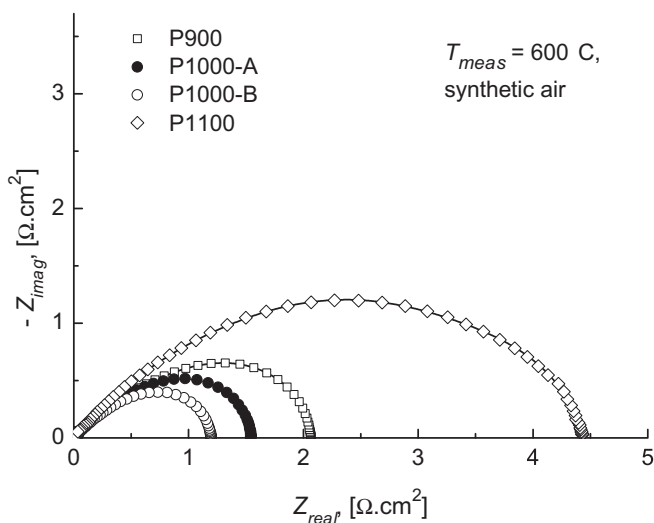

Fig. 5. Area specific electrode polarization impedance for the four symmetric cells, after subtraction of the apparent electrolyte resistance and instrumental inductance. The drawn lines represent the CNLS-modelling.

this sub-circuit is presented as (RQ)$_{hf}$, as its peak frequency is higher than for the Gerischer. The sample sintered at 1100 °C shows also a low frequency (RQ), where the CPE was close to capacitive behaviour ($n \approx 0.95$). This sub-circuit is presented as (RQ)$_{low}$ in Fig. 6. These two models could be used over the entire temperature and P_{O_2} range. In Fig. 6 both the measured data (closed circles) and the CNLS-fit (continuous line) are presented. The *separate* contributions of the Gerischer and the (RQ) sub-circuits, as obtained from the CNLS-analysis, are also presented (open symbols). The Gerischer parameters (Y_0, K_G) are directly obtained from the CNLS-analysis, see Eq. (2) with $Y_0 = Z_0^{-1}$. It can clearly be seen that the Gerischer dispersion has the largest contribution to the polarization resistance. The separate dispersions are presented as subsequent contributions, however between these there is significant overlap in the frequency spectrum. This is clearly demonstrated in Fig. 6D where for sample P1100 the separate contributions to the imaginary part are presented versus frequency. The summation of these separate imaginary dispersions is presented by the CNLS-fit which almost exactly falls on top of the measured data.

Fig. 7 shows the temperature dependence of the ASR of the four cells in synthetic air. For comparison the ASR for a similar symmetrical cell, measured by Sayers et al. [31], is also presented. These authors used the same type of CerPoTech powder, but a pre-processing step was applied before preparing the ink. This resulted in a starting powder with a 2 μm particle size, leading to a coarser microstructure. Furthermore, they applied a Pt-paint contact layer to the cathode to improve current collection. The overall activation energies obtained from the ASR of our samples range between 85 and 94 kJ mol^{-1}, see Table 1. The activation energy for the comparable sample by Sayers et al. [31] is 118 kJ mol^{-1}. The lowest ASR is obtained for samples sintered at 1000 °C with an ASR of $\sim$1.2 Ω cm^2 at 600 °C, about a factor 4–5 smaller than found by Sayers et al. [31], see the Discussion section.

Fig. 8 presents the Gerischer K_G parameters in an Arrhenius graph. The activation energies are $\sim$124 kJ mol^{-1} (Table 1). This is equal to the value of 124 kJ mol^{-1} obtained by Kilner and Shaw [32] for the overall exchange rate using oxygen isotope exchange. K_G also includes the thermodynamic factor, but its influence on the activation energy of K_G is minimal. Using Eqs (4), (5) and (10) and the calculated $\Re_0$ from Ref. [32] the K_G is calculated for the porous cathodes. Using the microstructure of sample P1100 (Fig. 2D) a rather conservative estimate of the specific surface area, a, is made with an average grain size of $\sim$560 nm and porosity of $\sim$40%, yielding: $a = 29 \cdot 10^3$ cm^2 cm^{-3}. The thus calculated K_G is also presented in Fig. 8. K_G for sample P1100 is still about a factor 8 smaller than the calculated value, but the used model does not include a tortuosity factor [14], nor a correction for 'dead-end' grains, which might be quite significant in this case.

It is remarkable that K_G increases with sintering temperature, while it is clear that the specific surface area, a, decreases in this respect. But also the tortuosity will decrease and the connectivity between grains will improve significantly with increasing sintering temperature. Nevertheless, the samples sintered at 1000 °C show the lowest ASR. It is remarkable that the K_G curves for these two samples exactly coincide, see Fig. 8.

A similar separate symmetric cell, prepared with LNO synthesized in our lab, showed also a Gerischer dispersion with an activation energy of $\sim$124 kJ mol^{-1} and with K_G close to that for the P1000 samples (not shown). Although the average grain size of 390 nm was comparable to the 340 nm for the P1000 samples, this sample showed a significantly larger ASR of 10 Ω cm^2 at 600 °C.

The temperature dependence of the normalized Gerischer Y_0 values (Z_0^{-1} from Eqs. (3) and (4)) are presented in Fig. 9. For the low temperature range ($<$600 °C) an Arrhenius type behaviour is observed, but at higher temperatures the curves bend over, which
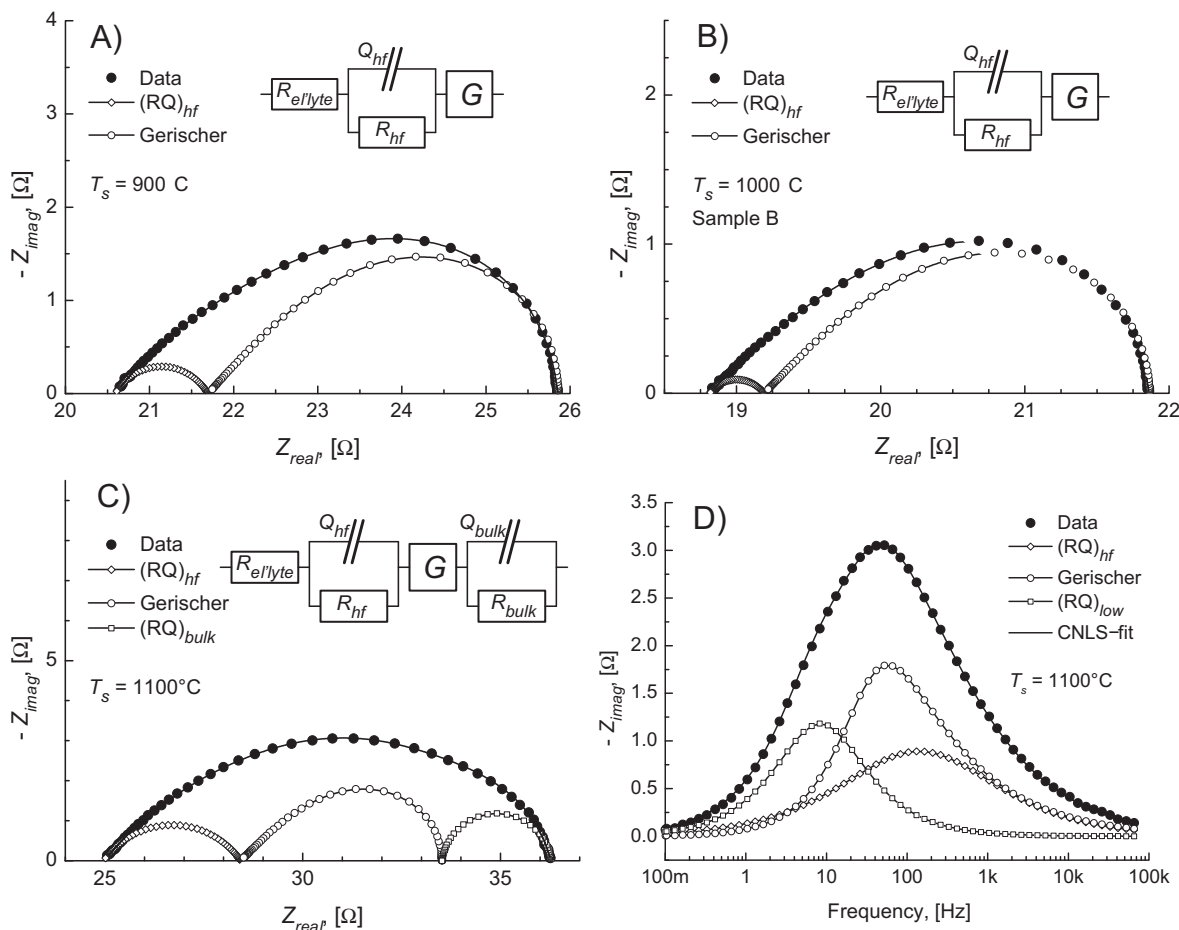
Fig. 6. Impedance diagrams with separate contributions of the Gerischer and (RQ) sub-circuits. Inserts: the equivalent circuits used in the CNLS analysis. $R_{el'lyte}$ is the apparent electrolyte resistance. A) Sample P900; B) sample P1000b; C) sample P1100. D) Separate sub-circuit contributions to Z_{imag} and overall fit for sample P1100.

might well be caused by the limited electronic conductivity of LNO. Again a simulated Y_0 is presented in Fig. 9. For this simulation the D_0 values, as presented in Refs. [25], are used with $D_O (T) = 1.47 \times 10^{-3} \exp(-83.8 \times 10^3/RT)$. Furthermore the previously mentioned results for the other materials parameters are used in Eq. (4), but only bulk transport of oxygen ions is assumed, ignoring

possible surface diffusion, i.e.: $\nu = 0$ in Eq. (4). There is an unexpected large difference between the simulated line and the measured values. This clearly suggests that the bulk diffusion is severely hampered by the 2-dimensional ionic conductivity and the observed microstructure (mostly sparsely connected single crystals, see Fig. 2). This discrepancy will be addressed further in the Discussion section. The average activation energy for the Arrhenius parts of the Gerischer Y_0 (T) curves is 32−39 kJ mol^{-1} (Table 1), while the apparent activation energy for the simulated curve is 37.7 kJ mol^{-1}.

At present there is no clear physical model for the (RQ)$_{hf}$ contributions. The corresponding values fall in a rather broad band in the Arrhenius representation of Fig. 10A. Considering the positions in this graph, it seems quite likely that the (RQ)$_{hf}$ are also dependent on microstructural parameters. The low frequency arc of cell
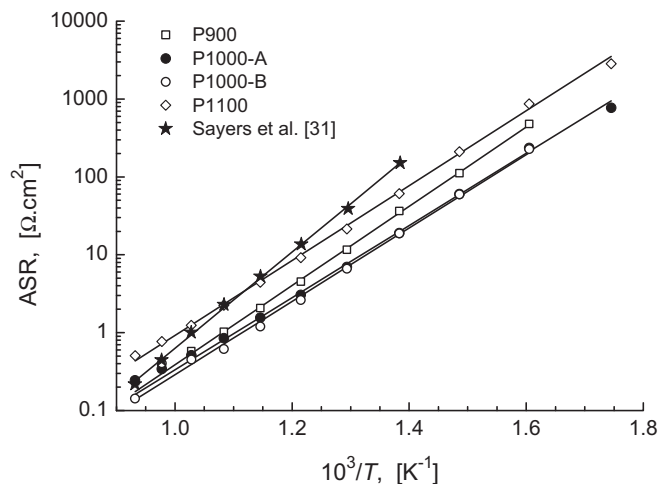
Fig. 7. Arrhenius graph of the ASR values for the porous cathodes, measured in synthetic air. The ASR for a symmetric cell by Sayers et al. [31] is shown for comparison.

Table 1
Compilation of the activation energies, in kJ mol^{-1}, for the fit parameters of the porous-type cells. For comparison the results for sample B of Sayers et al. in Ref. [31] is added. The error estimates are for a 1σ reliability interval.

Sample	ASR^{-1}	Gerischer-Y_0	Gerischer-K_G	R_{low}^{-1}
P900	93.6 ± 1.8	38.9 ± 1.4[a]	122.0 ± 0.5	n.a.
P1000-A	85.1 ± 1.7	32.2 ± 2.3[a]	124.5 ± 0.5	n.a.
P1000-B	88.6 ± 3.4	32.0 ± 0.9[a]	124.4 ± 0.7	n.a.
P1100	91.6 ± 1.2	36.4 ± 2.5[a]	118.4 ± 3.6	110 ± 4
Ref. [31]-B	118			

[a] Activation energy for the low-T part of the Gerischer-Y_0 curve, see Fig. 9.
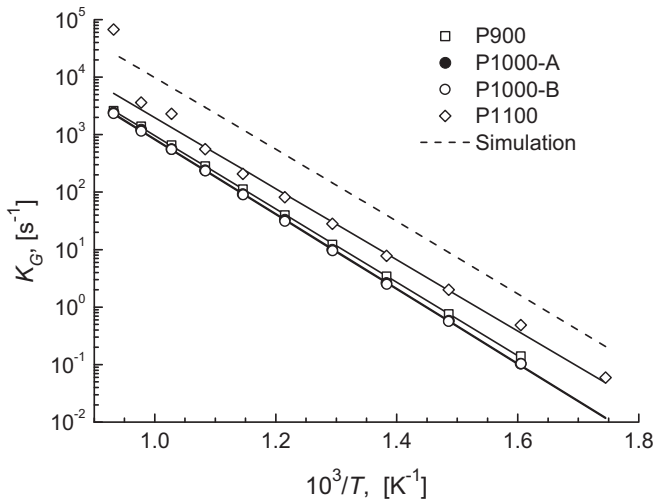
Fig. 8. Arrhenius graph of Gerischer K_G values for the four porous samples. The dashed line presents a simulation based on Eq. (5).

P1100, $(RQ)_{low}$, can be readily assigned to bulk redox behaviour of LNO, where R_{low} (see Fig. 10B) is a combination of bulk diffusion and surface exchange, as presented for thin layer behaviour in Eq. (9). But for these small sizes ($\sim 10^{-5}$ cm) it is most likely that R_{low} is related to the surface exchange rate only. The observed activation energy for R_{low} is ~ 110 kJ mol^{-1}, Fig. 10B. The low frequency CPE is transformed to an apparent capacitance, using the well-known relation [33,34]:

$$C_{app} = \frac{\sqrt[n]{R \cdot Y_0}}{R} \tag{11}$$

C_{app} is the apparent redox capacitance which is related to C_{chem} through Eqs. (8) and (9). Up to 600 °C this capacitance is almost constant, which is in accordance with $\ell \cdot k_{exch}/\tilde{D} << 1$. Based on this assumption an *effective* active layer thickness of ~ 50 nm is calculated, which for the porous structure would relate to the first few grains adjacent to the electrolyte.

The relatively low electronic conductivity of LNO is clearly demonstrated in Fig. 11. At low temperatures an Arrhenius type
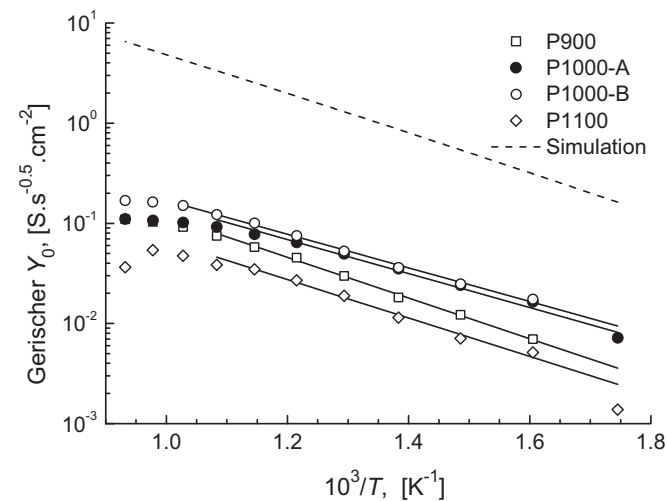

Fig. 10. Left: Compilation of the resistance contributions of the $(RQ)_{hf}$ sub-circuits for the porous samples. Right: Low frequency (RC) circuit parameters for the sample sintered at 1100 °C. The capacitance is calculated from Q_{low} using Eq. (11).

relation is observed for the apparent electrolyte resistance, but a serious deviation is seen with increasing temperatures which is due to the additional electronic resistance of the cathodes. For comparison the normalized resistance for a 100 μm thick TZ3Y electrolyte, prepared by ECN (Petten, the Netherlands) [33], is

Fig. 9. Arrhenius graph of the Gerischer Y_0 values for the porous cathodes. The linear parts in the Arrhenius graph are indicated. The simulation is based on Eq. (4), neglecting a possible contribution from surface diffusion.
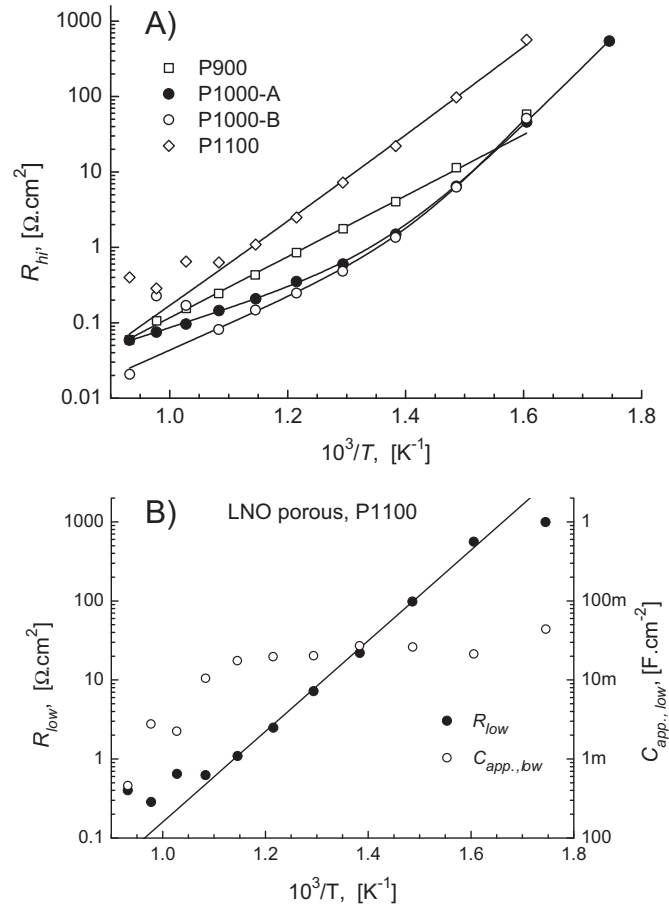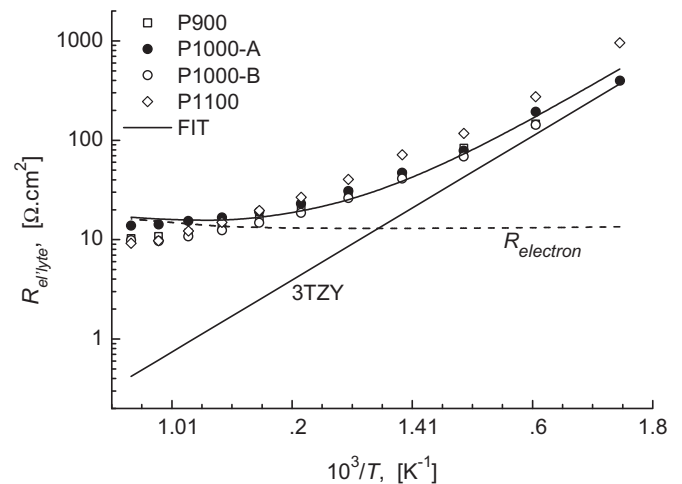

Fig. 11. Apparent electrolyte resistance for the porous symmetric cells. For comparison the normalized electrolyte resistance for 100 μm TZ3Y is included [27], as well as a fit of a combination $R_{electronic}$ for LNO [24] and R_{ionic} of TZ3Y.

presented. The fitted curve for cell P1000-A in Fig. 11 is the sum of the specific electronic resistance of LNO, multiplied by a 'matching factor', and the ionic resistance of TZ3Y. The area specific electronic resistance, calculated with the matching factor, is larger than expected for a ~50 μm thick porous cathode layer, i.e. at 600 °C about 5 Ω cm^2 observed versus 0.5–2 mΩ cm^2 estimated (based on results in Ref. [24]). This difference is due to the rather sparse electrical contact points provided by the Pt-grid (minimal 300 μm apart, or one contact per 0.09 mm^2), resulting in a significant sheet resistance contribution.

4.3. Impedance of porous cathodes, P_{O_2} dependence

The P_{O_2} dependence has been measured at 600 °C. Fig. 12 shows the Gerischer parameters as function of P_{O_2}. The Gerischer K_G shows a $(P_{O_2})^n$ dependence with $n \approx 0.5$, which is in agreement with the P_{O_2} dependence of 0.5 as observed for the isotope exchange rate of LNO, obtained through pulsed isotope exchange (PIE) measurements (Bouwmeester and Yoo, [35]). The Gerischer Y_0 values are virtually independent of P_{O_2} as indicated by the horizontal lines (average values) in Fig. 12. In the temperature and pressure range used, the P_{O_2} dependence of the thermodynamic factor is given by (Eq. (11)): $d \ln P_{O_2}/d \ln\delta \propto \delta$. Provided that the model by Eq. (4) may still be applied and assuming that the oxygen self-diffusion coefficient, D_O (with $D_i \approx 4 \cdot D_O/\delta$), is also virtually independent of P_{O_2} (or δ), the δ-dependencies in Eq. (4) will cancel. Hence G-Y_0 will be P_{O_2} independent as a consequence. As a result, the P_{O_2} dependence of the Gerischer contribution to the polarization goes with $(P_{O_2})^{-1/4}$, see Eq. (3), but due to the other contributions the order of the P_{O_2} dependence of the polarization resistance is about −0.27 (cells P900 & P1100) and −0.305 (cells P1000-A & -B). The apparent low frequency capacitance for P1100 shows a small P_{O_2} dependence (order: ~−0.1 ± 0.05), which is a small deviation from the prediction by Eq. (9), i.e. P_{O_2} independence. For the corresponding resistance, $R_{low} \propto (P_{O_2})^{-0.4}$ is found. For all samples the apparent electrolyte resistance shows a small P_{O_2} dependence, which is due to a contribution of the p-type electronic conductivity of the LNO electrodes.

4.4. Impedance of thin layer modified cathodes

Fig. 13 shows the normalized impedance for the four 'DP-type' cells with the apparent electrolyte resistance and instrumental inductance removed. The shape is clearly different from that of the
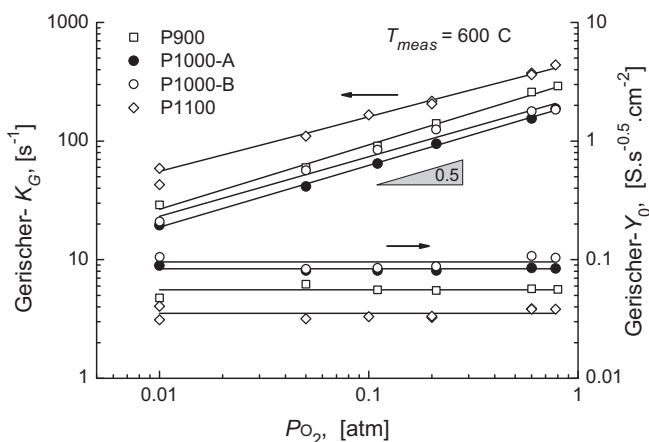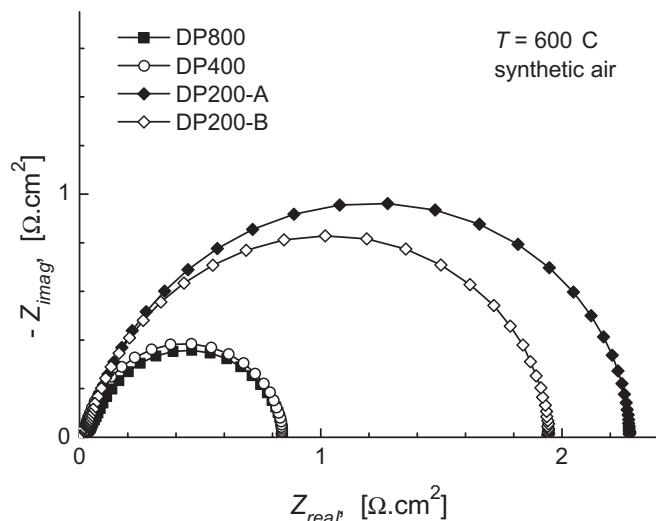

Fig. 13. Comparison of the polarization impedances of the 'DP-type' samples. The apparent electrolyte resistance and inductance have been subtracted from the dispersion data.

porous electrode cells, Figs. 5 and 6, and is dominated by a low frequency (RQ)-type dispersion, which is analyzed further down. The samples DP200-A and -B and DP400 show also small Gerischer contributions in the CNLS-analysis, but these can only be retrieved with acceptable accuracy in a limited temperature range. The normalized polarization resistance or ASR is presented in Fig. 14. The best ASR for the standard porous sample P1000 is also shown for comparison, together with the results published by Sayers et al. [31] for a similar symmetric cell with dip-coated dense LNO layers of ~2 μm (cell C of Ref. [31]). The thin dense base-layers clearly improve the overall performance of the LNO cathodes. The apparent activation energies of the ASR's are in the range 87–96 kJ mol^{-1} and are presented in Table 2.

The apparent electrolyte resistance for the DP-samples (not shown) is also affected by the relatively low electronic conductivity, although overall the effect is somewhat smaller than for the porous samples. This is to be expected due to an increased contact area between electrolyte and electrode (from ~40% for the porous samples to nearly 100% for the dense/porous samples).

Fig. 12. P_{O_2} Dependence of the Gerischer parameters (K_G, Y_0) for the porous samples. A slope of $(P_{O_2})^{0.5}$ is indicated. Horizontal lines are averages of the Y_0 values.
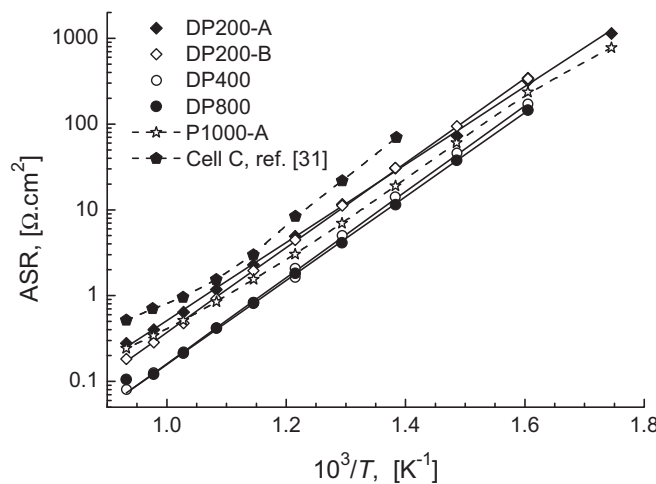

Fig. 14. Compilation of the ASR for the 'DP-type' samples, measured in synthetic air. For comparison the ASR of the porous ($T_s = 1000$ °C) sample is included, as well as a similar dense/porous cell by Sayers et al. ([31] cell-C).

Table 2
Compilation of the activation energies, in kJ mol^{-1}, for the fit parameters of the dense/porous-type cells. The error estimates are for a 1σ reliability interval.

| Sample	ASR^{-1}	R_{layer}^{-1}	Gerischer-K_G
DP200-A	87 ± 1	89.6 ± 1.2	93.8 ± 4.4[a]
DP200-B	94.5 ± 0.8	96.4 ± 0.6	102 ± 7[a]
DP400	95.9 ± 1.1	94.2 ± 1.1	94.2 ± 1.3
DP800	92.8 ± 0.6	94.0 ± 0.9	n.a.

[a] These values were estimated in the 450–650 °C temperature range.

The CPE (Q_{low}) of the major dispersion is close to being capacitive ($n \approx 0.94$–0.98) and represents the apparent chemical capacitance, C_{app}, Eq. (8). The resistance of the $(RQ)_{\text{low}}$ circuit represents the exchange resistance of the layer, R_{layer}, Eq. (8). The normalized R_{layer} values are close to the presented ASR values in Fig. 14. Observed activation energies for the ASR and R_{layer}, are, with $E_{\text{act}} = 90$–96.5 kJ mol^{-1}, significantly lower than the overall surface exchange rate of 124 kJ mol^{-1}, see Table 2. The apparent chemical capacitance decreases rapidly with increasing temperature as shown in Fig. 15, which indicates that at low temperatures the surface exchange is too slow, i.e. the layer acts as a redox or battery electrode. With increasing temperature the surface exchange path becomes more dominant, resulting in an increase in the $\ell \cdot k_{\text{exch}}/\tilde{D}_O$ term in Eq. (8). As both K_G and $\tilde{D}_O$ are thermally activated, this term can be described by a single activation energy. According to literature the activation energy of the oxygen exchange process is higher than that of the oxygen bulk diffusion [25,32]. Modelling of C_{app} for DP800, with the C_{chem}-volume and $x = \ell \cdot k_{\text{exch}}^{\circ}/\tilde{D}_O$ as adjustable parameters, yields a quite reasonable fit with E_{act} ~29 kJ mol^{-1} for DP800 and ~36 kJ mol^{-1} for DP400. Fig. 15 clearly indicates that at lower temperatures the redox (or battery electrode) activity, C_{chem}, includes also a part of the porous electrode structure, as the effective specific capacitance is higher than the theoretical value which is calculated on basis of the thin PLD layer only.

4.5. Impedance of thin layer modified cathodes, P_{O_2} dependence

For the two samples with the thinnest PLD layer, DP200-A & -B, identical results were obtained. The apparent chemical capacitance showed a very small P_{O_2} dependence with: $C_{\text{app}} \propto (P_{O_2})^{0.06\pm0.02}$, close to being P_{O_2} independent (Eq. (9)). The order in P_{O_2} for R_{layer} is around -0.30 ± 0.05 (DP200-A) and -0.40 ± 0.02 (DP200-B). The
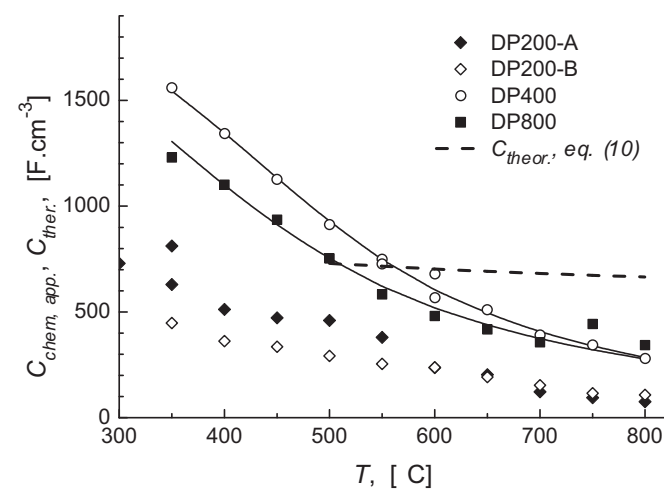
Fig. 15. Evolution of the apparent chemical layer capacitances with temperature. For DP400 and DP800 a simulation, based on Eq. (9), is added. The theoretical chemical capacitance, C_{chem}, using the δ-values of Ref. [24], is also presented.

K_G parameter of the Gerischer contribution has a clear $(P_{O_2})^{0.5}$ dependence: 0.50 ± 0.03, identical to what was observed for the porous samples. The Gerischer-Y_0 parameter is, within the experimental error limits, virtually independent of the oxygen partial pressure for the DP200 and DP400 samples. In contrast with the DP200 samples, the Gerischer K_G for the DP400 sample is also, within the experimental error limits, independent of P_{O_2}. The C_{app} for both the DP400 and DP800 cells is also virtually independent of P_{O_2}.

5. Discussion

There are several publications on the surface exchange rate, oxygen diffusion, non-stoichiometry and electronic conductivity for LNO. Unfortunately there is quite some disagreement between these publications. Bassat et al. [36] have studied the oxygen exchange and diffusion in single crystal LNO, clearly showing the anisotropic nature of this compound. Sayers et al. [37] have recently studied the oxygen isotope exchange and tracer diffusion coefficient on dense ceramic samples in the temperature range of 350–700 °C. They found a much lower activation energy of 61 ± 7 kJ mol^{-1} for k_{exch} than from a previous study [32]. In Table 2 of this recent paper a summary of published values for D^* and k^* is presented [37]. The value of 124 kJ mol^{-1}, as observed in our study, is further supported by the study of the impedance of a 300 nm thin LNO film by Kim et al. [38]. They found ~127 kJ mol^{-1} for the surface oxygen exchange rate. Using a 'pulsed isotope exchange' method (PIE, [20]) Bouwmeester et al. determined a value ~141 kJ mol^{-1} for the overall exchange rate.

But also on the determination of the non-stoichiometry there is little agreement. We have chosen for the non-stoichiometry determinations by Naumovitch et al. [23] and Kharton et al. [24] as these present a complete range of δ-values as function of temperature (650–950 °C) and oxygen partial pressure ($10^{-4} - 0.7$ atm). Values reported by Sayers and Skinner [39], measured by TGA at a P_{O_2} of 0.21 atm are significantly higher. Those measured by Sayers et al. [37], using iodometric titration, also show in the range 350–550 °C higher values for δ with a large statistical error. In contrast, δ-values calculated by Kim et al. from the thin layer impedance and those obtained for LNO powders [38] are substantially smaller than presented by Refs. [23,24]. Confirmation of the non-stoichiometry measurements by Naumovitch and Kharton [23,24] is needed, but also thorough determination of other materials properties of LNO will help in accurately modelling the performance of LNO cathodes.

Several studies have also been presented on the performance of LNO cathodes for use in solid oxide fuel cells. The results by Sayers et al. [31], who used the same type CerPoTech LNO powder, but with a processing step, have been used as comparison for our results. At first glance it seems that a cathode structure with a large specific surface area (cm^2 cm^{-3}) significantly lowers the ASR. This clearly points to the importance of surface diffusion in the oxygen reduction step. Escudero et al. [40] studied the oxygen reduction kinetics of the LNO cathode with EIS. They used a set of three (RQ)'s in series to model their data. An activation energy of 116 kJ mol^{-1} was found with an ASR (600 °C) of 58 Ω cm^2. Pérez-Coll et al. [41] studied the effect of electrolyte type on the performance of the porous LNO cathode. They also used a three (RQ) model to analyze the data. The best results were obtained for 40 mol% Sm-doped ceria. The activation energy of the ASR was 134 kJ mol^{-1} with an ASR (600 °C) of 21 Ω cm^2. In both cases the LNO powder was prepared through a citrate synthesis. But also the impedance data obtained by Sayers et al. [31] for CerPoTech LNO cathodes were analyzed with a three (RQ) circuit. Hence our results for the porous cathodes show a distinctly different electrode process with a Gerischer dispersion as main component of impedance.

The modelling of the Gerischer, Figs. 8 and 9, shows especially for the Gerischer-Y_0 parameter a significant deviation from the experimental values if only bulk oxygen transport is assumed. This difference for the P1000 cells of a factor of 20–25 could be explained by a strongly reduced 'effective' bulk diffusion coefficient, due to the 2-D diffusion and the special microstructure. But it can also be explained by a surface diffusion model where oxygen adsorbs dissociatively on the LNO surface forming mobile O_{ad}^- species (see e.g. Ref. [41]). The diffusion equations would then become:

$$J = -D_s \frac{d\Gamma\theta(x)}{dx} \tag{12}$$

where J is the flux at the triple phase boundary (TPB, $x = 0$), D_s is the surface diffusion coefficient, Γ the number of adsorption sites per cm^2 and θ the occupancy by O_{ad}^- species, which is assumed to be small: $\theta << 1$. The amount of adsorbed O_2 is assumed to be negligible. As $\theta(x)$ will change locally due to the surface diffusion, the exchange reaction will yield a net flux, adding an extra term to Fick's second law:

$$\frac{d\Gamma\theta(x)}{dt} = D_s \frac{d^2\Gamma\theta(x)}{dx^2} - K_{dis}\left[\Gamma\theta(x) - \Gamma\theta^\circ\right] \tag{13}$$

with K_{dis} the rate for dissociative adsorption (which is virtually equal to the overall exchange rate as the incorporation rate is generally much faster [42]) and θ° the equilibrium occupation. The second boundary condition is semi-infinite diffusion:

$$\lim_{x \to \infty} \theta(x) = \theta^\circ \tag{14}$$

It is useful to write $\theta(x)$ as a perturbation, θ_x, of the equilibrium value: $\theta(x) = \theta^\circ + \theta_x$. The voltage, as measured at the TPB, then reads (with one electron transfer per O_{ad}^-):

$$V_{x=0} = \frac{RT}{F}\ln\frac{\theta^\circ + \theta_x}{\theta^\circ} \approx \frac{RT}{F\theta^\circ}\theta_x \tag{15}$$

Applying Laplace transforms to Eqs. (12)–(15) and setting the Laplace variable equal to $j\omega$ results in an Gerischer type impedance expression for surface diffusion, with ℓ_{TPB} the TPB-length per unit area:

$$Z_{surf}(\omega) = \frac{RT}{F^2 \cdot \ell_{TPB} \cdot \Gamma\theta^\circ \sqrt{D_s}} \cdot \frac{1}{\sqrt{K_{dis} + j\omega}} \tag{16}$$

Under the assumption that the transfer of the second electron to form $O_{ad}^-(O_2 + \Gamma(1-\theta) + e \rightarrow O_{2,ad}^-$, followed by: $O_{2,ad}^- + \Gamma(1-\theta) + e \rightarrow 2O_{ad}^-)$ is the slowest step, it follows that $\theta \div (P_{O_2})^{1/4}$, see Ref. [42]. Hence the Gerischer-Y_0 should also show a $(P_{O_2})^{1/4}$ dependence. But the surface gradient in $\theta(x)$ will also cause oxygen transfer between adsorption and lattice sites. As there is as yet insufficient knowledge about the parameters governing this process it will not be further elaborated in this contribution.

The ASR values for our best porous samples (P1000-A and -B) at 600 °C, resp. 1.5 and 1.2 Ω cm^2, are significantly lower than those in literature. This indicates that smaller grain sizes improve the electrode performance. The sintering temperature, T_s, is of significant importance; a too low temperature creates a fine microstructure with a large surface area, but with poor adherence to the electrolyte, i.e. a poorly defined TPB. Increasing T_s results in an improved 'footprint' of the electrode and hence a better TPB and bulk contact, but due to an increasing grain size the specific surface area decreases. Hence, these 'opposing' processes lead to an optimum value for the sintering temperature.

The addition of a dense base-layer increases the electrode performance further, with an ASR (600 °C) of $\sim$0.85 Ω cm^2 for DP400 and DP800. But it also dramatically changes the electrode process. The dispersion is now controlled by the thin layer properties. The rather fine grain size ($\sim$100 nm) in this layer ensures good ionic conductivity, which is in contrast with the property of the porous structure. A thicker layer does not increase the ASR, the layer resistances are identical for DP400 and DP800, which supports the assignment of R_{layer} to the surface exchange process. If surface diffusion is assumed as the major transport process for the porous electrodes, then the charge transfer in the TPB zone will be the rate limiting factor. Adding a dense layer will then provide an extended charge transfer zone over the entire surface area exposed to the ambient. This will improve the diffusion related process, e.g. smaller Gerischer contributions as observed, but it will add the thin layer dispersion as an additional electrode contribution. The identical layer resistances for DP400 and DP800 indicate that the electronic conductivity is sufficient to support the surface oxygen transfer at the ambient/layer interface. A restriction by the electronic conduction would lead to a thickness dependent R_{layer}.

The layer related impedance, $(RQ)_{low}$ qualitatively follows the model predictions of Eqs. (8) and (9). It is assumed that the Gerischer (DP200 and DP400) or the $(RQ)_{high}$ dispersion for DP800 can be added in series with the layer dispersion, $(RQ)_{low}$. Proper modelling needs to be performed with e.g. a Finite Element Method (see for example Ref. [45]), but then it is essential that reliable materials properties are available.

The R_{layer} for DP400 and DP800 represents clearly the oxygen transfer rate at the ambient/layer interface. The activation energy ($\sim$94 kJ mol^{-1}) is significantly lower than for the overall exchange rate, K_G (124 kJ mol^{-1}), obtained from the porous samples. A tempting, tentative model is to associate this R_{layer} with transfer of surface adsorbed mono-atomic oxygen species into the bulk (and visa versa). This idea is based on the two-step exchange model as proposed in Refs. [19,20]. Assuming O_{ad}^- to be the active species, a single electron transfer per oxygen is needed, hence the incorporation exchange rate, k_i, can then be expressed by:

$$k_i = \frac{RT}{F^2 c_{ox}^\circ \cdot S \cdot R_{layer}} \tag{17}$$

where S is the surface area. Taking for S the geometrical surface area, k_i is obtained for DP400 and DP800 and displayed in the Arrhenius graph, Fig. 16. As, besides the rather rough surface of the dense layer, also some grains of the porous structure will be involved in this transfer process the effective surface area, S, may still be underestimated. For comparison the overall exchange rate from IEDP measurements (Kilner et al. [32]) and the overall exchange rate, k_0, and bulk exchange, k_i, rate from PIE measurements (Bouwmeester et al. [20]) are also presented in Fig. 16. Interesting is the position of k_0, obtained from EIS measurements by Kim et al. [38]. Röntgen analysis of the thin PLD layer indicated a certain degree of preferential orientation with the c-axis in the plane of the layer. Hence the surface with the ambient is well-aligned for optimal exchange, which could explain the higher k_0 value with respect to the isotope exchange data [20,32].

The emerging picture of the oxygen reduction mechanism can be described as follows: surface diffusion of (most likely) charged oxygen species is the major step for fine grained porous electrodes. Due to the 2-D restricted bulk ion conduction the second reduction step takes place at a (poorly defined) triple phase boundary, which creates a bottleneck for the total oxygen transfer, see the left-hand cartoon in Fig. 17. This process leads to a Gerischer dispersion, where k_d is the adsorption/dissociation rate (E_{act} = 124 kJ mol^{-1}). As this is the slowest step in the exchange process, it is virtually
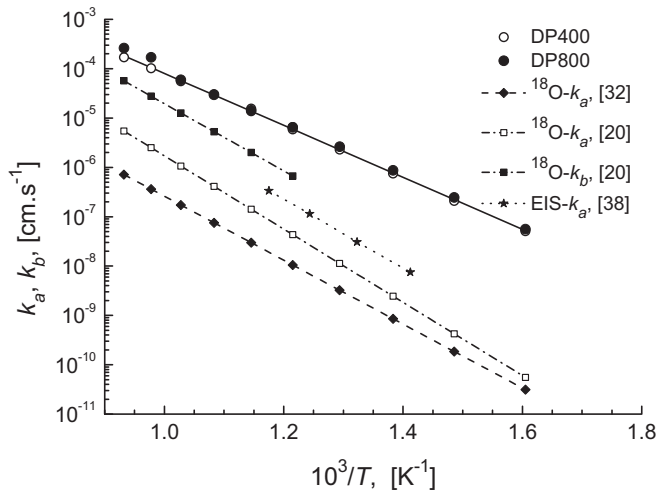
Fig. 16. Comparison of the exchange coefficient, k_b, in [cm s^{-1}] as obtained from R_{layer} for DP400 and DP800, and the overall exchange coefficient, k_0, by Kilner and Shaw (IEDP, [32]). For the PIE measurements by Bouwmeester et al. [20] both exchange coefficients, k_0 and k_i, are presented. The EIS measurements by Kim et al. [38] were performed on a 300 nm thin LNO layer: R_3 has been converted to k_0.

equal to the overall exchange rate: $k_0^{-1} = k_d^{-1} + k_i^{-1}$. 'Inserting' the dense layer between electrolyte and the porous structure effectively enhances the TPB to the entire exposed layer surface, providing a large area for electron transfer in the incorporation reaction. Oxygen dissociation over the large surface area of the porous structure and the fast diffusion of adsorbed oxygen species can sustain a significant flow to the dense layer surface, where the charge transfer and lattice incorporation reaction now becomes the rate determining step, as depicted in the right-hand cartoon of Fig. 17. This is the second exchange reaction step, which is faster than the dissociation step (for equal size surface area) and which has lower activation energy, as clearly shown in Fig. 16. For the DP200 samples there still is a transition from the porous model to the layer + porous model. Of course, the presented model is too simple to explain all observed features of the impedance analysis, however the suggested model explains semi-quantitatively the most important observations.

Finally, LNO was selected as a potentially Cr-poisoning resistant cathode material. Whether this actually is the case still remains to be seen. Another Ni-based material, the LaNi$_{0.6}$Fe$_{0.4}$O$_3$ perovskite, was also suggested as a cathode material with the promise of being Cr-resistant. However, extensive testing showed that Ni is expelled from the perovskite structure by gaseous Cr-species, most likely in the form of NiO. As a result a Cr-based perovskite shell is formed on
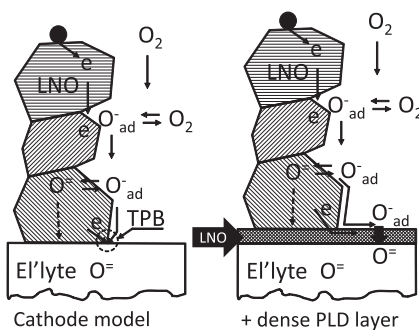
the crystallites, causing significant degradation of the performance over time [43,44].

6. Conclusions

- For a proper modelling of the electrode reactions it is essential that reliable materials properties, such as diffusion and exchange parameters and non-stoichiometry as function of T and P_{O_2}, are available. Currently there is a significant discrepancy between results from different research groups.
- The 2-D ionic conductivity causes a serious constraint on the electrode performance. Surface diffusion appears to be the dominant oxygen transport path for porous LNO cathodes, as indicated by a significant Gerischer dispersion in the electrode impedance.
- A higher sintering temperature results in an improved contact between porous electrode and electrolyte and better connectivity between the grains. But at the same time the specific surface area of the electrode decreases. For the used CerPoTech powder this results in an optimum sintering temperature of ∼1000 °C for the lowest ASR.
- Insertion of a dense base-layer between electrolyte and porous electrode structure is advantageous for the electrode properties. It improves the electrode footprint, lowers the sintering temperature and enlarges the TPB region. Here the ASR (600 °C) was decreased by ∼35% with respect to the best porous cell.
- A semi-quantitative, tentative model is presented, which is based on the two-step oxygen exchange model. It explains the significant shift in the electrode reaction on introduction of a dense LNO base-layer.
- The electronic conductivity of LNO is too low. An additional top layer with high electronic conductivity (e.g. a Pt paint layer) is needed to avoid the current distribution problem.

Acknowledgements

Fig. 17. Cartoons explaining the difference in the oxygen reduction path for a standard porous LNO-cathode (left) and a base-layer modified cathode (right). The hatching of the LNO grains depicts the random orientation of the 2-dimensional ionic conduction planes.

References

[1] W.J. Quadakkers, H. Greiner, M. Hänsel, A. Pattanaik, A.S. Khanna, W. Malléner, Solid State Ionics 91 (1996) 55–67.
[2] S.P. Jiang, S. Zhang, Y.D. Zhen, J. Electrochem. Soc. 153 (2006) A127–A134.
[3] D. Oh, E. Armstrong, D. Jung, C. Kan, E. Wachsman, ECS Trans. 25 (2009) 2871–2879.
[4] S.P. Simner, M.D. Anderson, M.H. Engelhard, J.W. Stevenson, Electrochem. Solid-State Lett. 9 (2006) A478–A481.
[5] M. Yang, E. Bucher, W. Sitte, Proceeding. 9th European SOFC Forum, June 29–July 2, 2010.
[6] T. Komatsu, R. Chiba, H. Arai, K. Sato, J. Power Sources 176 (2008) 132–137.
[7] S.J. Skinner, J.A. Kilner, Solid State Ionics 135 (2000) 709–712.
[8] H. Zhao, F. Mauvy, C. Lalanne, J.-M. Bassat, S. Fourcade, J.-C. Grenier, Solid State Ionics 179 (2008) 2000–2005.
[9] C. Laberty, Z. Feng, K.E. Swider-Lyons, A.V. Virkar, Electrochem. Solid-State Lett. 10 (2007) B170–B174.
[10] F. Mauvy, C. Lalanne, J.-M. Bassat, J.-C. Grenier, H. Zhao, L. Huo, P. Stevens, J. Electrochem. Soc. 153 (2006) A1547–A1553.
[11] M. Rieu, R. Sayers, M.A. Laguna-Bercero, S.J. Skinner, P. Lenormand, F. Ansart, J. Electrochem. Soc. 157 (4) (2010) B477–B480.
[12] N. Hildenbrand, B.A. Boukamp, P. Nammensma, D.H.A. Blank, Solid State Ionics 192 (2011) 12–15.
[13] B.A. Boukamp, H.J.M. Bouwmeester, Solid State Ionics 157 (2003) 29–33.
[14] S.B. Adler, J.A. Lane, B.C.H. Steele, J. Electrochem. Soc. 143 (1996) 3554–3564.
[15] Y. Lu, C. Kreller, S.B. Adler, J. Electrochem. Soc. 156 (2009) B513–B525.
[16] S. Carter, A. Seluk, R.J. Chater, J. Kaida, J.A. Kilner, B.C.H. Steele, Solid State Ionics 53–56 (1992) 597–605.
[17] B.A. Boukamp, Solid State Ionics 135–137 (2000) 75–82.
[18] B.A. Boukamp, Solid State Ionics 143 (2001) 47–55.

[19] B.A. Boukamp, K.J. de Vries, A.J. Burggraaf, in: J. Nowotny, W. Weppner (Eds.), Non-Stoichiometric Compounds; Surfaces, Grain Boundaries and Structural Defects, NATO ASI Series C: Mathematics and Physical Sciences, vol. 276, Kluwer Academic, Dordrecht, 1989, pp. 299–309.

[20] H.J.M. Bouwmeester, C. Song, J. Zhu, J. Yi, M. van Sint Annaland, B.A. Boukamp, Phys. Chem. Chem. Phys. 11 (2009) 9640–9643.

[21] C.-Y. Yoo, B.A. Boukamp, H.J.M. Bouwmeester, J. Solid State Electrochem. 15 (2011) 231–236.

[22] B.A. Boukamp, N. Hildenbrand, P. Nammensma, D.H.A. Blank, Solid State Ionics 192 (2011) 404–408.

[23] E.N. Naumovich, M.V. Patrakeev, V.V. Kharton, A.A. Yaremchenko, D.I. Logvinovich, F.M.B. Marques, Solid State Sci. 7 (2005) 1353–1362.

[24] V.V. Kharton, E.V. Tsipis, E.N. Naumovich, A. Thursfield, M.V. Patrakeev, V.A. Kolotygin, J.C. Waerenborgh, I.S. Metcalfe, J. Solid State Chem. 181 (2008) 1425–1433.

[25] E. Boehm, J.-M. Bassat, P. Dordor, F. Mauvy, J.-C. Grenier, Ph. Stevens, Solid State Ionics 176 (2005) 2717–2725.

[26] G. Amov, S.J. Skinner, J. Solid State Electrochem. 10 (2006) 538–546.

[27] C. Ferchaud, J.-C. Grenier, Y. Zhang-Steenwinkel, M.M.A. van Tuel, F.P.F. van Berkel, J.-M. Bassat, J. Power Sources 196 (2011) 1872–1879.

[28] B.A. Boukamp, J. Electrochem. Soc. 142 (1995) 1885–1894.

[29] B.A. Boukamp, Solid State Ionics 20 (1986) 31–44.

[30] A. Wisse, B.A. Boukamp, EqCwin95, http://www.wisseq.nl/portfolio.aspx, (in Dutch).

[31] R. Sayers, M. Rieu, P. Lenormand, F. Ansart, J.A. Kilner, S.J. Skinner, Solid State Ionics 192 (2011) 531–534.

[32] J.A. Kilner, C.K.M. Shaw, Solid State Ionics 154–155 (2002) 523–527.

[33] T. Jacobsen, B. Zachau-Christiansen, L. Bay, S. Skaarup, in: F.W. Poulsen, N. Bonanos, S. Linderoth, M. Mogensen, B. Zachau-Christiansen (Eds.), Proceedings of the 17th Risø International Symposium on Materials Science, Risø National Laboratory, Roskilde, Denmark, 1996, p. 29.

[34] C.S. Hsu, F. Mansfeld, Corrosion 57 (2001) 747–748.

[35] H.J.M. Bouwmeester, C.-Y. Yoo, unpublished results.

[36] J.M. Bassat, P. Odier, A. Villesuzanne, C. Marin, M. Pouchard, Solid State Ionics 167 (2004) 341–347.

[37] R. Sayers, R.A. De Souza, J.A. Kilner, J.S. Skinner, Solid State Ionics 181 (2010) 386–391.

[38] G.T. Kim, S. Wang, A.J. Jacobson, Z. Yan, C. Chen, J. Mater. Chem. 17 (2007) 1316–1320.

[39] R. Sayers, S.J. Skinner, J. Mater. Chem. 21 (2011) 414–419.

[40] M.J. Escudero, A. Aguadero, J.A. Alonso, L. Daza, J. Electroanal. Chem. 611 (2007) 107–116.

[41] D. Pérez-Coll, A. Aguadero, M.J. Escudero, P. Núñez, L. Daza, J. Power Sources 178 (2008) 151–162.

[42] B.A. Boukamp, I.C. Vinke, K.J. de Vries, A.J. Burggraaf, in: B. Scrosati, A. Magistris, C.M. Mari, G. Mariotto (Eds.), Fast Ion Transport in Solids, NATO ASI Series E: Applied Sciences, vol. 250, Kluwer Academic, Dordrecht, 1993, pp. 167–180.

[43] M.K. Stodolny, B.A. Boukamp, D.H.A. Blank, F.P.F. van Berkel, J. Power Sources 196 (2011) 9290–9298.

[44] M.K. Stodolny, B.A. Boukamp, D.H.A. Blank, F.P.F. van Berkel, J. Power Sources 209 (2012) 120–129.

[45] D. Herbstritt, A. Weber, E. Ivers-Tiffée, J. Eur. Ceram. Soc. 21 (2001) 1813–1816.

List of symbols with units

Γ: number of adsorption sites [cm^{-2}]

δ: non-stoichiometry parameter [−]

ε: degree of porosity [−]

θ: degree of occupancy of adsorption sites [−]

θ^0: equilibrium value of θ [−]

ω: radial frequency, $\omega = 2\pi f$ [s^{-1}]

a: effective surface area [cm^{-1}]

A^0: thermodynamic factor [−]

c_O: lattice oxygen concentration [mol cm^{-3}]

C_{app}: apparent chemical capacitance [F cm^{-3}]

C_{chem}: chemical or redox capacitance [F cm^{-3}]

$\tilde{D}_O$: chemical diffusion coefficient of oxygen ions [cm^2 s^{-1}]

D_O, D_v, D_i: self-diffusion coefficient of oxygen ions, vacancies and interstitials, resp. [cm^2 s^{-1}]

D_s: surface diffusion rate [cm s^{-1}]

J: flux [mol cm^{-2} s^{-1}]

K_G: Gerischer reaction rate [s^{-1}]

K_{dis}: (chemical) dissociative adsorption rate, Eq. (13) [s^{-1}]

k_0: overall oxygen exchange rate, $k_0^{-1} = k_d^{-1} + k_i^{-1}$ [cm s^{-1}]

k_d: dissociative adsorption rate [cm s^{-1}]

k_i: oxygen incorporation rate [cm s^{-1}]

k_{exch}: chemical exchange rate, $k_{exch} = k_0 \cdot (1/2)(\partial \ln P_{O_2}/\partial \ln \delta)$ [cm s^{-1}]

ℓ: layer thickness [cm]

P_{O_2}: oxygen partial pressure [atm]

$\Re_0$: overall surface exchange rate, $\Re_0 = c_O \cdot k_0$ [mol cm^{-2} s^{-1}]

S: surface area [cm^2]

V_m: molar volume (based on one formula unit) [cm^3 mol^{-1}]

x_v^0, x_i^0: mole fraction of oxygen vacancies, ∼interstitials [−]

Y_0, Z_0: frequency independent part of the admittance, ∼impedance, dimension depends on type of dispersion equation